

See discussions, stats, and author profiles for this publication at: <https://www.researchgate.net/publication/326848441>

# Development of a Portable Electrical Impedance Tomography System for Biomedical Applications

Article in IEEE Sensors Journal · October 2018

DOI: 10.1109/JSEN.2018.2864539

CITATIONS

0

READS

562

7 authors, including:



Jiafeng Yao

Nanjing University of Aeronautics & Astronautics

44 PUBLICATIONS 72 CITATIONS

SEE PROFILE



Yanli Liu

Nanjing University of Aeronautics & Astronautics

5 PUBLICATIONS 1 CITATION

SEE PROFILE

Some of the authors of this publication are also working on these related projects:



Kinematics, Dynamics of the Parallel Mechanisms [View project](#)



Biomedical Measurement with Electrical Impedance Tomography [View project](#)

# Development of a Portable Electrical Impedance Tomography System for Biomedical Applications

Zifei Xu, Jiafeng Yao, Zheng Wang, Yanli Liu, Hao Wang, Bai Chen, Hongtao Wu

**Abstract**—A portable Electrical Impedance Tomography (EIT) system has been developed with Red Pitaya STEMLab for biomedical applications. The Red Pitaya STEMLab is a portable device to realize voltage generation and data acquisition for the EIT system. The EIT system includes a modified howland circuit as a voltage controlled current source (VCCS), a high speed analogy multiplexer module, 8-electrode array and a personal computer. The Generalized Vector Sampled Pattern Matching (GVSPM) algorithm and the Tikhonov (TK) regularization algorithm are used to reconstruct the image generated by the EIT system. The reconstructed images by using Red Pitaya STEMLab are compared with a commercial impedance analyzer IM3570 within frequencies of  $f = 100$  KHz. The results show that the maximum difference of the image correlation between Red Pitaya STEMLab and IM3570 is 5.36%. Finally, the EIT system are used to image the conductivity of eggs during heating process. These results verified that the developed portable EIT system with Red Pitaya STEMLab could measure the biological tissue in a high accuracy at low cost.

**Index Terms**—Electrical Impedance Tomography, Portable device, Red Pitaya STEMLab, Image correlation.

## I. INTRODUCTION

Electrical Impedance Tomography (EIT) is widely used in biomedical field because of its advantages of low cost, fast response, safety, no radiation, and non-invasiveness [1, 2]. The biological tissue consists of cells that can be modeled as electrical components. The concentration and size of the cells can be distinguished by resistance, capacitance and relaxation frequency characteristics of the electric double layer (EDL) exhibited by the cell membrane under current excitation [3].

Manuscript received \*\*\*\*; revised \*\*\*\*; accepted \*\*\*\*. Date of publication \*\*\*\*; date of current version \*\*\*\*. This work was supported by the National Natural Science Foundation of China (51706098), the Natural Science Foundation of Jiangsu Province (BK20170792), the Natural Science Research of Jiangsu Higher Education Institutions of China (17KJB460003) and the Science and Technology Planning Project of Guangdong Province, China (2017A020215134). (Corresponding author: Jiafeng Yao.)

Z. Xu, J. Yao, Z. Wang, Y. Liu, B. Chen, H. Wu are with the College of Mechanical & Electrical Engineering, Nanjing University of Aeronautics & Astronautics, Nanjing 210016, China (e-mail: jiaf.yao@nuaa.edu.cn).

H. Wang is with the department of Anesthesiology, the First Affiliated Hospital of Jinan University, Guangdong 510632, China.

Color versions for one or more of the figures in this paper are available online at \*\*\*\*.

Digital Object Identifier \*\*\*\*.

The impedance information of the biological tissue can be reflected by the Alternating Current (AC) characteristic of the biological tissue. EIT is a technique to reconstruct the images of the biological tissue distribution by using the difference in electrical conductivity inside a biological tissue. The image of the conductivity distribution is reconstructed by injecting a safe AC signal into the electrodes on the biological surface and measuring the potentials of the remaining electrodes on the biological surface [4].

A lot of meaningful work has been conducted by researchers to improve the quality of the reconstructed images [5-9]. Since EIT systems require sophisticated measuring instruments, the image quality of the traditional EIT is limited by hardware. EIT experimental setup includes high speed analog multiplexer and impedance analyzer [10]. High speed analog multiplexer is used as electrode switches to connect electrodes and signal input/output channels [11]. Impedance analyzers is used to generate and acquire signals. The advantages of impedance analyzer are high measurement accuracy and ease of use, but it is bulky and expensive. Most impedance analyzers do not conform to the electrical safety standards of human measurement because they are mainly used to measure resistance, inductance and capacitance circuits [12]. Therefore, the use of EIT system composed of impedance analyzer is limited to laboratories and hospitals and cannot be widely used in families and individuals.

In recent years, several novel EIT are designed including mfEIT system [13], Sheffield Mk3.5 EIT/EIS system [14], UCLH Mk2.5 EIT system [15], KHU Mark2.5 EIT system [16], 16-electrode wireless Electrical Impedance Tomography (EIT) system [17]. Among these systems, mfEIT system has high-frame-rate data acquisition and is used as real-time 2D and 3D imaging. Sheffield Mk3.5 EIT/EIS system frequency ranges up to  $f = 1.6$  MHz, the average signal to noise performance of the system is 40 dB measured across all frequencies. UCLH Mk2.5 EIT system is small and compact and has an error within  $\pm 0.7\%$  over the frequency range 20 Hz to 256 KHz. KHU Mark2.5 EIT system can maintain SNR of 80 dB at up to 250 KHz, and the reciprocity error within 24 hours is less than 0.5%. These systems generally have high frequency range and good performance.

However, most of the systems described above are expensive and complex. Biological tissues detection by EIT does not require very high frequencies. For example, the frequency of

the excitation signal required for hand gesture recognition is  $f = 40$  kHz [18], and the frequency of excitation signal required for lung monitoring is  $f = 50$  KHz [19]. At this point, impedance analyzer can be easily replaced by some low-cost devices. Red Pitaya STEMLab is an experimental and measurement instrument platform that has the advantages of ease of use, high performance-to-price ratio, and excellent performance.

This paper is to develop a portable, low-cost EIT measurement system with Red Pitaya STEMLab. Firstly, the hardware of the EIT system with eight electrodes is designed by using Red Pitaya STEMLab, a high output impedance voltage controlled current source (VCCS) and a high speed analog multiplexer module. Secondly, the image reconstruction algorithm of EIT selects the generalized vector sampled pattern matching (GVSPM) algorithm and Tikhonov (TK) regularization algorithm, and the conditions for obtaining the best image of GVSPM are studied by experiments. Next, the performance of the developed portable EIT system is verified by the comparison with EIT system by using the high-precision impedance analyzer IM3570. Finally, the developed EIT is used to image eggs during heating process.

## II. HARDWARE DEVELOPMENT

The EIT system adopts a modular design, mainly including Red Pitaya STEMLab, a high output impedance voltage controlled current source (VCCS) which consisting of a modified howland circuit, a high speed analog multiplexer module, an electrode sensor array, and a personal computer (PC). Red Pitaya STEMLab contains a Matlab programmable FPGA module. The PC sends a command to Red Pitaya STEMLab to generate an AC voltage signal. The VCCS module is used to convert the AC voltage signal generated by Red Pitaya STEMLab into a stable AC current signal with the same frequency. The current signal is injected into one pair of electrodes outside the field through the analog multiplexer module. The voltage signals of the other electrode pairs are collected into Red Pitaya STEMLab through the analog multiplexer module, and then transferred to PC for data processing and image reconstruction using Matlab. The overall structure of the EIT system is shown in Fig. 1.

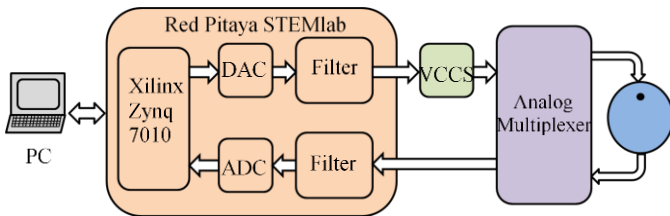


Fig. 1. The overall structure of the EIT system

### A. Application of Red Pitaya STEMLab

The commercial Red Pitaya STEMLab can fulfill most of the functions of the EIT system. In the EIT system Red Pitaya STEMLab is not only responsible for the data exchange with the PC, but also for voltage signal processing, including signal generation and acquisition, analog-to-digital conversion and digital-to-analog conversion, amplification, and low-pass

filtering. The hardware of the Red Pitaya STEMLab consists of a dual-core ARM processor, interface devices, and an FPGA (Xilinx Zynq 7010 SOC) supports software and hardware programming.

The analog front-end of Red Pitaya STEMLab has a  $2 \times 125$  MS/s fast analog output RF channels and a  $2 \times 125$  MS/s fast analog input RF channels, both with 50 MHz analog bandwidth. The frequency of output signals can be set to  $f = 0$  Hz to  $f = 50$  MHz. The amplitude of the generated analog signal is within  $V = \pm 1$  V. Input stage of fast analog inputs can be used for two voltage ranges ( $\pm 1$  V and  $\pm 20$  V). The principle of signal acquisition is to pass the input signal through a low-pass filter and then through an analog-to-digital converter to write to the data buffer in the FPGA chip. When the data buffer is full of new signals, the buffer is terminated. The data buffer can store up to 16384 signal values, but at the same time, the sampled data is also stored in memory, which will increase the recording capacity to millions of samples.

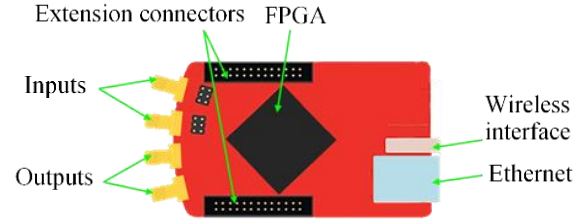


Fig. 2. Red Pitaya STEMLab

Red Pitaya STEMLab is controlled remotely through LAN or wireless interface using Matlab through Standard Commands for Programmable Instrumentation (SCPI) list of commands. PC in EIT system uses Matlab to control Red Pitaya STEMLab through wireless connection. Matlab is a powerful data analysis tool and supports SCPI commands that can retrieve data stored in Red Pitaya STEMLab. The code for EIT is written in Matlab to control the FPGA and CPU so that the application on the EIT can be developed on the PC. The Red Pitaya STEMLab has 16 digital input/output channels at a voltage of  $V = 3.3$  V, which can be used as address inputs for analog multiplexers. The signal generation and processing ability of Red Pitaya STEMLab can realize many functions of EIT system.

### B. Voltage Controlled Current Source Development

EIT system adopts the method of injecting current and measuring voltage, because the current source is safer for the human body than the voltage source [20]. The ideal current source internal resistance should be infinite, and will not change due to changes in temperature and load. Many articles have conducted indepth research on current sources and have proposed many current sources for EIT, such as Improved Howland circuit [20-22], current mirror circuit [23], General Impedance Converter circuit [24]. Howland circuit is a classic voltage controlled current source circuit, and the feasibility of using Modified Howland circuit in EIT system has been proved [25, 26]. Bertemesfilho et al. shows that there is no significant difference in the actual application results between the Modified Howland current source and the current mirror structure [24].

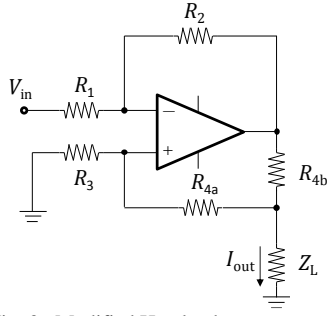


Fig. 3. Modified Howland current source

The Modified Howland current source is shown in Fig. 3. It has lower power loss than the earlier Howland current source. The advantage of Modified Howland compared to other current sources is that it does not use additional transistors or switches and the disadvantage is that the resistance in its circuit is difficult to match.

Modified Howland current source has a positive feedback circuit and a negative feedback circuit, and equilibrium conditions of the feedback circuit is given by:

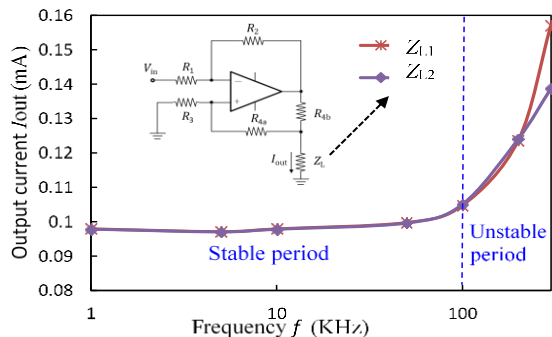
$$R_2/R_1 = (R_{4a} + R_{4b})/R_a \quad (1)$$

When (1) is satisfied, the output resistance of the circuit  $R_{out} = \infty$ , of the output current is given by:

$$I_{out} = R_2 V_{in} / (R_1 R_{4b}) \quad (2)$$

When (1) is satisfied, the output current is determined by the ratio of the resistors in the circuit and the input voltage, regardless of the load  $Z_L$ . The installation of high-precision and low-temperature drift resistors in the circuit to reduce the effects of resistance changes on output current and output impedance.

In the design of VCCS in this paper, when the input voltage signal amplitude is  $V_m = 1$  V, theoretically the corresponding output current is  $I_{out} = 0.1$  mA. The experimental conditions were set as follows: the load are  $Z_{L1} = 2$  K $\Omega$ ,  $Z_{L2} = 4$  K $\Omega$  and the input voltage signal amplitude is  $V_m = 1$  V. The measured output current of the Howland current source at different frequencies is shown in Fig. 4, which indicates that the output current is around  $I_{out} = 0.1$  mA when the current source frequency is in the range of  $f = 1$  KHz to  $f = 100$  KHz.

Fig. 4. The relationship between output current  $I_{out}$  and frequency  $f$ 

The output impedance is an important performance index of

VCCS and represents the stability of the output current to different load impedance. The output impedance of the circuit is severely degraded in the high frequency range due to the presence of the output capacitor  $C_{out}$  in the circuit. The test method for VCCS output impedance is as follows: the outputs of the VCCS are connected in series with different load resistors  $Z_{L1} = 2$  K $\Omega$  and  $Z_{L2} = 4$  K $\Omega$ , at a frequency of  $f = 100$  KHz. The voltages  $V_1$  and  $V_2$  of the resistors  $Z_{L1}$  and  $Z_{L2}$  are measured respectively, and the output impedance of the VCCS is calculated by (3). After calculation, at frequency  $f = 100$  KHz, the output impedance of VCCS is  $Z_{out} = 726$  K $\Omega$ , which is greater than  $Z_{out} = 100$  K $\Omega$  required by EIT system [27]. The biological tissue can be measured from the frequency  $f = 10$  KHz to  $f = 100$  KHz, so this VCCS meets the EIT usage requirements [28].

$$Z_{out} = (V_2 - V_1) / (V_1/Z_{L1} - V_2/Z_{L2}) \quad (3)$$

Biological tissue can achieve EIT in the range of frequency  $f = 10$  KHz – 100 KHz [28]. For example, the imaging of the electrical impedance of the arm can be detected at the frequency  $f = 40$  KHz [29]. VCCS has a high output impedance ( $Z_{out} > 100$  K $\Omega$ ) in the frequency range  $f = 100$  KHz, which meets the requirements for biological tissue measurements.

### C. Analog Multiplexer Module Development

The high speed analog multiplexer module in the EIT system is used to connect the electrodes and signal input/output channels. The four-electrode method is used to avoid the effects of electrode polarization in the experiment. By injecting excitation current signals through two adjacent electrodes, the voltage signals between the other adjacent electrode pairs are alternately collected, as shown in Fig. 5. Then the current signals are injected into the next adjacent pair of electrodes, and the voltage signals on other adjacent electrodes pairs are collected. Repeat the previous process until all adjacent electrode pairs are rotated. Using the 8-electrode EIT system of the adjacent method, a total of forty measurements were obtained.

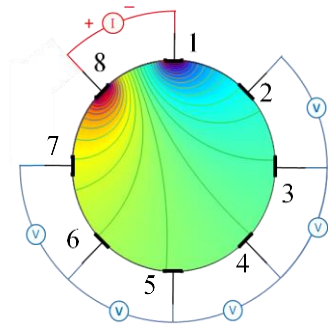


Fig. 5. Measurement approach in one cross-section

Each measurement requires two electrodes to connect two signal input channels high current (HC) and low current (LC) respectively, and two electrodes to connect two signal output channels high potential (HP) and low potential (LP) respectively. The EIT system uses the CD74HC4067 devices to

form a high speed analog multiplexer module for channel switching. The CD74HC4067 device is a high speed analog multiplexer with sixteen independent inputs/outputs (Y0 to Y15) and a common input/output (Z).

The high speed analog multiplexer module with four CD74HC4067 devices is shown in Fig. 6. Common inputs/outputs (Z) on the devices are connected to high current (HC), low current (LC), high potential (HP), and low potential (LP), respectively. The address inputs (S0 to S3) on the devices are connected to the digital output channels of Red Pitaya, and the Y0 to Y7 channels of the 16 independent inputs/outputs channels are connected to the 8-sensor electrodes outside the measured field.

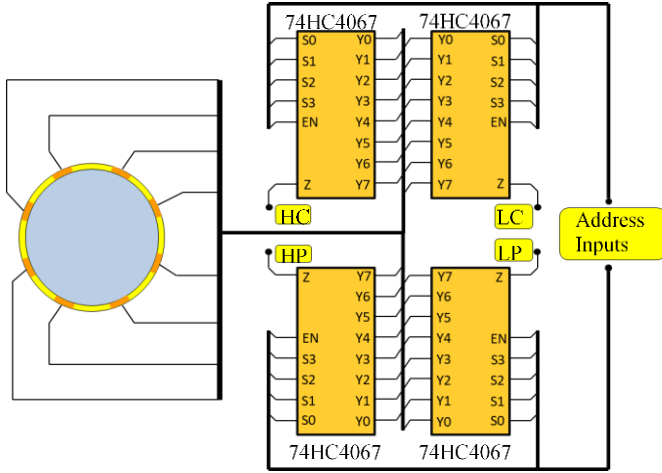


Fig. 6. The analog multiplexer module

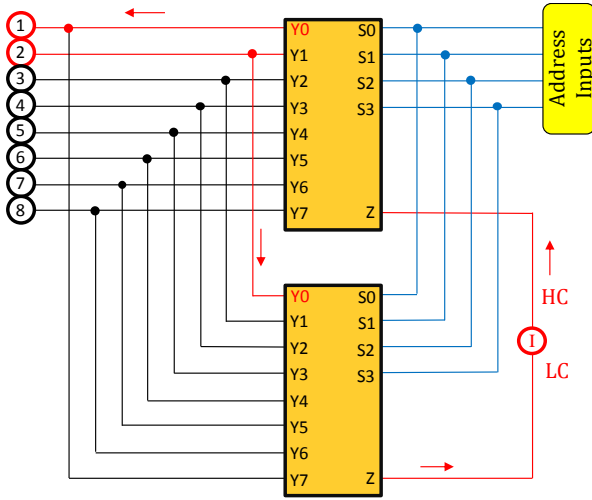


Fig. 7. Electrode pair 1-2 input a current signal

A Matlab program is used to control the potential of the address inputs (S0 to S3) of the four CD74HC4067 devices connected to the digital output channels of the Red Pitaya STEMLab, and determine which electrodes are connected to the HC, LC, HP, and LP, respectively. Among them, two devices connected with HC and LC have the same address inputs. As shown in Fig. 7, the address inputs of both devices are low (S0 = S1 = S2 = S3 = L), then HC and LC are connected to Y0 channels respectively (Y0 = HC, Y0 = LC). However, the two

Y0 channels are not connected to the same electrode but are connected to the electrodes 1 and 2 according to the electrode excitation mode. This allows two devices to be simultaneously controlled by four address inputs (S0 to S3) to connect HC and LC to adjacent electrode pairs. The other two devices wiring the same way. The EIT system can control four devices simultaneously through the eight digital output channels of Red Pitaya STEMLab, rather than sixteen digital output channels.

#### D. Practical Phantom design

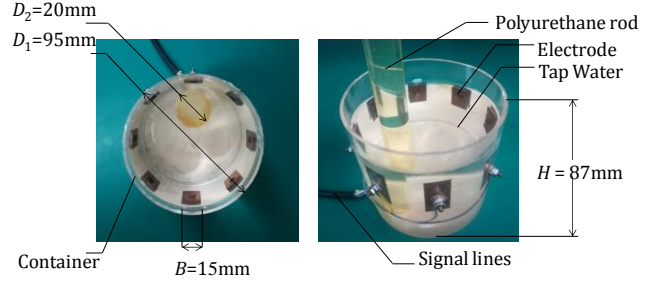


Fig. 8. Practical phantom with eight electrodes

A practical phantom with eight electrodes was designed for experimentation and imaging. The physical phantom was tested and researched in the laboratory, which proved that the EIT system designed in this paper can basically achieve the goal of distinguishing different conductivity objects in the water tank. As shown in Fig. 8, the diameter of the flume is  $D_1 = 95$  mm, and the height is  $H = 87$  mm. There are eight pieces of electrode with a width of  $B = 15$  mm and a length of  $L = 30$  mm, which are evenly distributed near the inner wall. The internal solution is tap water that has been left for one hour at a temperature of  $T_1 = 25$  °C, and forty voltage values can be obtained by measuring according to the adjacent method described above. Then a polyurethane rod with a diameter of  $D_2 = 20$  mm is placed in the water, and forty boundary voltage values after the impedance distribution change can be obtained without changing the original measurement environment. The two sets of data are used as input data for the image reconstruction algorithm.

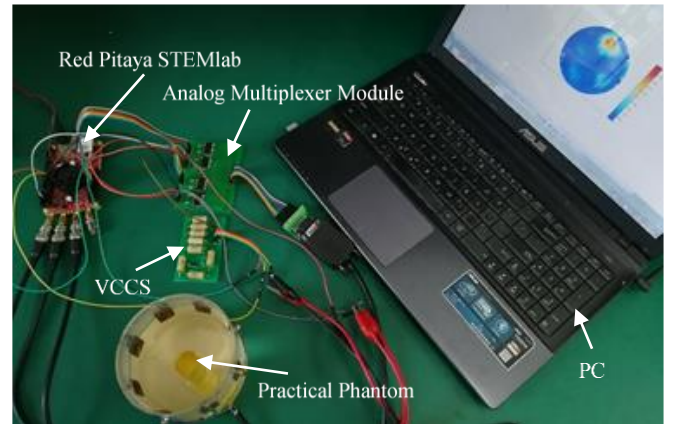


Fig. 9. The picture of the EIT hardware system

The EIT system designed in this paper adopts a modular design with a simple structure. Others can also follow this model and easily design a suitable and protable EIT hardware system using Red Pitaya STEMLab. Table I contains the



comparison of the specifications of the designed EIT system and the impedance analyzer.

TABLE I  
COMPARISON OF THREE DEVICE SPECIFICATIONS

Device	Developed EIT	HIOKI IM3570	Agilent E4990A
Frequency Resolution	1 Hz	0.01 Hz	0.001 Hz
Frequency Range	0~100 KHz	4 Hz~5 MHz	20 Hz~120 MHz
Connect	Wired / Wireless	Wired	Wired
Volume & Weight	110×28×60mm <sup>3</sup> 0.1 kg	330×119×307mm <sup>3</sup> 5.8 kg	432×235×277mm <sup>3</sup> 14 kg
Price	About \$400	Over \$10000	Over \$24000

### III. EXPERIMENTAL METHODS AND CONDITIONS

#### A. Image reconstruction algorithm

The inverse problem of EIT is mostly reduced to an equation for solving an ill-posedness system, and the solution of the equation is not unique. The image reconstruction algorithm used in this paper are Tikhonov (TK) regularization and Generalized Vector Sampled Pattern Matching (GVSPM). Tikhonov regularization algorithm is more popular in solving EIT inverse problems [30]. However, Tikhonov regularization need artificially set a regularization factor  $\mu$ , and  $\mu$  is an empirical factor that has a great influence on the quality of image reconstruction [31]. GVSPM is an algorithm for solving linear equations through iteration. GVSPM is a target criterion based on the minimum angle between the input vector and the solution vector, which can effectively overcome the drawbacks of the iterative algorithm. The GVSPM solution contains an objective function and can converge without any empirical value. It is an iterative solver that can be used in most ill-posed linear systems, and is very suitable for image reconstruction of EIT [31, 32]. The objective function  $F$  of the  $k$ -th iterative particle distribution  $\sigma^{(k)}$  is given by:

$$F = f(\sigma^{(k)}) = U'^{(exp)} \cdot U'^{(k)} \rightarrow 1.0 \quad (4)$$

Where  $U^{(exp)}$  denotes the voltage vector measured through experiment,  $U^{(k)}$  denotes the voltage vector obtained through the  $k$ -th iteration,  $(')$  denotes the normalized quantities.

#### B. Conductivity distribution of the simulation model

The electrical conductivity distribution of the simulation model is a criterion for evaluating the quality of the practical phantom reconstructed image. In order to obtain the conductivity of the simulation model, it is necessary to establish the equivalent geometric model of the homogenous field (the interior of the field contains only tap water) and the non-homogeneous field (the interior of the field includes tap water and Polyurethane rod, as shown in Fig. 8) in software. The finite element method (FEM) is used to split the geometric

model into finite triangular elements, as shown in Fig. 10 (a) and (b). The geometry model of homogeneous field is used to calculate the positive problems and sensitivity matrix of EIT. The geometry model non-homogeneous field is used to obtain simulated conductivity distributions. The conductivity distribution of the heterogeneous field simulation model is shown in Fig. 10 (c).

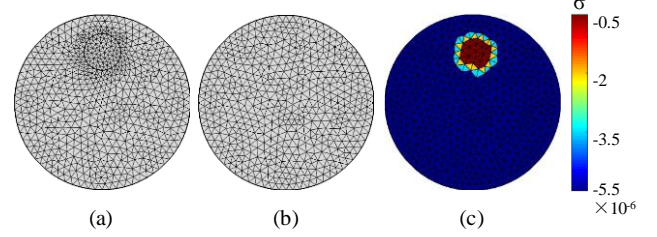


Fig. 10. (a) Mesh of geometric model of the non-homogenous field (b) Mesh of homogeneous geometry model (c) Conductivity distribution of simulation model

#### C. Image quality evaluation

Voltage error  $U_E$  is a criterion to evaluate the voltage vector  $U^{(k)}$  in the  $k$ -th iteration of GVSPM, given by:

$$U_E = \sqrt{\sum_{i=1}^n (U_i^{(k)} - U_i^{(exp)})^2} / \sqrt{\sum_{i=1}^n (U_i^{(exp)})^2} \quad (5)$$

where,  $U_i^{(k)}$  is the  $i$ -th element of  $U^{(k)}$ ,  $U_i^{(exp)}$  is the  $i$ -th element of  $U^{(exp)}$ . The Pearson correlation coefficient is the evaluation standard to reflect the image correlation  $I_C$  of the conductivity distribution obtained by the experimental measurement and simulation.  $I_C$  is a value between +1 and -1, where  $I_C = 1$  is total positive linear correlation,  $I_C = 0$  is no linear correlation, and  $I_C = -1$  is total negative linear correlation. The greater the absolute value of  $I_C$ , the more similar the electrical conductivity distribution of the two is, and the closer the measured conductivity distribution is to the true value. The calculation formula of  $I_C$  is:

$$I_C = (\sum(\alpha - \bar{\alpha})(\sigma - \bar{\sigma})) / \sqrt{\sum(\alpha - \bar{\alpha})^2 \sum(\sigma - \bar{\sigma})^2} \quad (6)$$

Where  $\alpha$  and  $\sigma$  are the conductivity of the model in software and the conductivity measured in experiment, respectively.  $\bar{\alpha}$  and  $\bar{\sigma}$  are the average of  $\alpha$  and  $\sigma$ , respectively.

### IV. EXPERIMENTAL RESULTS AND DISCUSSION

#### A. Optimum iteration number

Ideally, in the GVSPM algorithm, the objective function  $F$  gradually goes to 1 as the number of iterations  $Iter$  increases.  $I_C$  is an index for evaluating the quality of the reconstructed image, and the larger the better. The voltage error  $U_E$  is a criterion for evaluating the voltage vector  $U^{(k)}$  obtained in the  $k$ -th iteration of the GVSPM, and the smaller the better. The practical phantom shown in Fig. 8 is measured by the EIT system at the frequency  $f = 10$  KHz, and the voltage of the electrode is collected to reconstruct the image. The relationship between  $Iter$  with  $F$ ,  $I_C$ , and  $U_E$  respectively is shown in Fig. 11. The

objective function  $F$  rises rapidly after a sharp drop, then slowly increases and converges. The change trend of  $U_E$  is the opposite of  $F$ , but there is a clear trough at  $Iter = 16$ . The value of  $I_C$  also changed dramatically during the previous iteration, and gradually decreased as the number of iterations increased after the peak. The peak of  $I_C$  appears near the first trough of  $U_E$ .

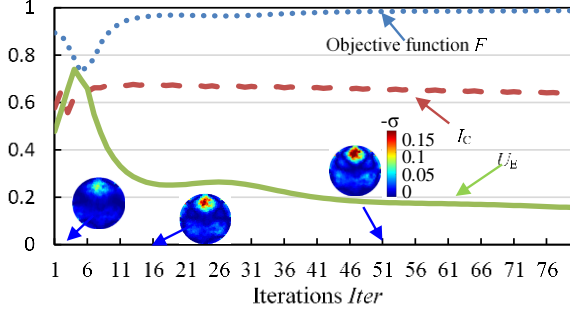


Fig. 11. Relationship between  $Iter$  with  $F$ ,  $I_C$  and  $U_E$  respectively

### B. Single target multi-frequency imaging experiment

Experiments were performed on the single-target practical phantom shown in Fig. 8 at frequencies  $f = 1$  KHz, 10 KHz, 50 KHz, 100 KHz, 200 KHz, 300 KHz, and 400 KHz to verify the theory obtained from experiment A and test the performance of the EIT system. Fig. 12 shows how the image correlation  $I_C$  and voltage error  $U_E$  of the reconstructed image with the increase of number of iterations  $Iter$  when  $f = 1$  KHz, 10 KHz, 50 KHz, and 100 KHz. When the voltage error  $U_E$  reaches the first trough, all  $I_C$  get the optimal value. Next, the voltage error  $U_E$  is used as a criterion for judging whether the iteration is completed or not, and the image correlation  $I_C$  is used as a criterion for evaluating the quality of the reconstructed image when the GVSPM algorithm is used to reconstruct the image.

The electrode potential is measured at the boundary of the field and GVSPM is used to reconstruct the conductivity distribution inside the field for the collected data. Red Pitaya STEMLab is used to generate and acquire signals in the EIT

system. The image correlation  $I_C$  of the conductivity distribution measured by the actual phantom shown in Fig. 8 and the conductivity distribution of the simulation model are compared at different frequencies, and the result is shown in Fig. 13.

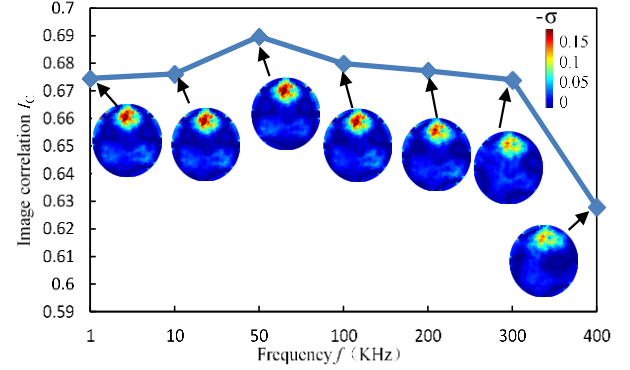


Fig. 13. Image correlations at different frequencies

Fig. 13 shows that the EIT system designed in this paper can be used to reconstruct images of single target practical phantom at multiple frequencies, but the effect of reconstructing images is different. The EIT system can accurately image the polyurethane rod phantom within the frequency  $f < 300$  KHz, and the image correlation  $I_C$  of the conductivity distribution image is large. The size and position of practical phantom can be distinguished from the image, but the shape of practical phantom is not well reflected in the image. Combining the conductivity distribution of the simulation model, this is due to the fact that the finite element meshing is not fine enough and the measurement error appears. However, if the density of the finite element mesh is increased, the ill-posedness of the inverse problem of EIT will increase. When the frequency  $f > 300$  KHz, the reconstructed image correlation  $I_C$  becomes smaller and the image becomes unclear, but the position of practical phantom is still distinguished. On the one hand, the impedance of the polyurethane rod becomes lower as the

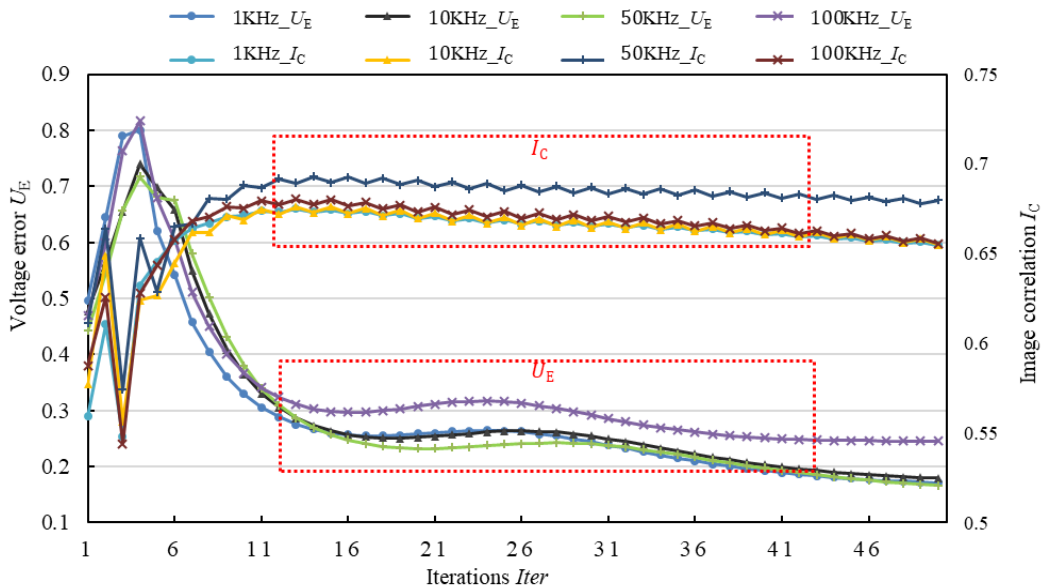


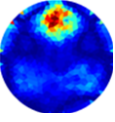
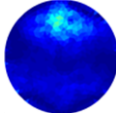
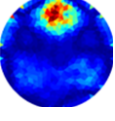
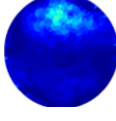
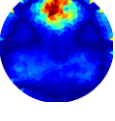
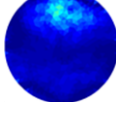
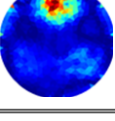
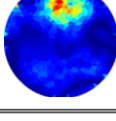
Fig. 12. Relationship between  $Iter$  with  $I_C$  and  $U_E$  respectively

frequency increases. On the other hand, the noise of the line at a high frequency will have a serious influence on the measurement result, making the measurement accuracy lower. The experiment used 8-electrode phantom, which can improve the imaging effect by increasing the number of electrodes to 16-electrode [33].

### C. Impedance analyzer imaging experiment

The single target practical phantoms shown in Fig. 8 were imaged at the frequencies  $f = 1$  KHz, 50 KHz, and 100 KHz using an impedance analyzer IM3570 instead of the Red Pitaya STEMLab and VCCS in the system. Table II shows the image correlation  $I_C$  and the reconstructed image obtained in the two modes. The images reconstructed in both modes reflect the size and position of the polyurethane rod, and all have strong image correlation  $I_C$ . The correlation  $I_C$  of the image reconstructed by the impedance analyzer is precedence, and the correlation  $I_C$  of the reconstructed image using Red Pitaya STEMLab and VCCS has the maximum change at the frequency of  $f = 100$  KHz, which is 5.36%. These results show that the two models of EIT systems can accurately image the polyurethane rod phantom within  $f = 100$  KHz.

TABLE II  
RECONSTRUCTED IMAGE AND IMAGE CORRELATION

Red Pitaya STEMLab		Impedance Analyzer		Frequency
Image	Image Correlation	Image	Image Correlation	
	0.6745		0.6953	1 KHz
	0.6761		0.6730	10 KHz
	0.6897		0.7090	50 KHz
	0.6799		0.7184	100 KHz

### D. Application to Biomedical Imaging

The developed EIT system was used to reconstruct the images of raw egg and heated egg separately. Reconstructing the image with the TK algorithm is more suitable for responding to the difference in the conductivity of the raw egg and heated egg compared to using the GVSPM. The regularization factor  $\mu = 10^{-7}$ .

First, the image of the raw egg in the container is reconstructed at ambient temperature  $T_1 = 25$  °C. Then, the raw egg was heated in  $T_2 = 100$  °C boiling water and taken out after different heating times ( $t = 1$  min, 4 min, 8 min, 16 min). The

heated egg was cooled rapidly with flowing cold water to ambient temperature  $T_1 = 25$  °C and placed in the container for image reconstruction. The distribution of the conductivity of the egg after different heating times is shown in Fig. 14.

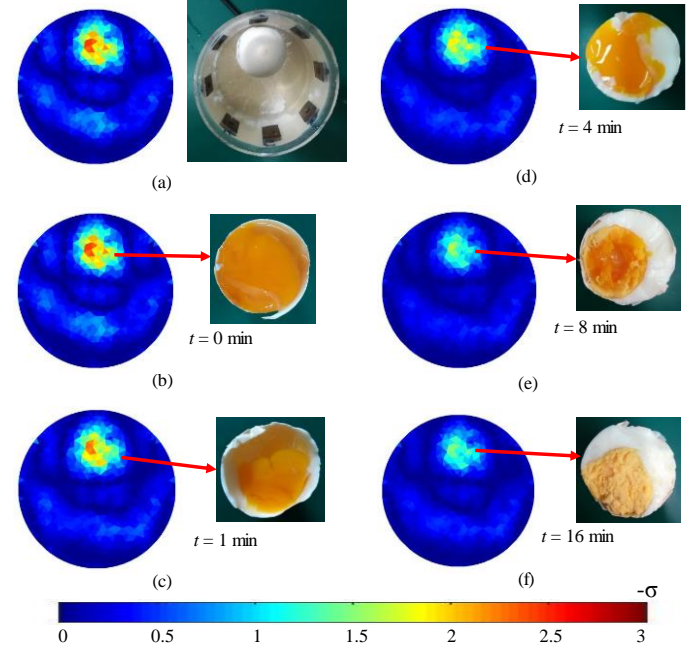


Fig. 14. Reconstructed Image of egg at 50 KHz (a, b) Reconstructed images of raw egg (c, d, e, f) Reconstructed images of egg heated for  $t = 1$  min, 4 min, 8 min and 16 min, respectively

Fig.14 shows that the conductivity of the egg is closer to that of tap water as the heating time  $t$  increases. This is because the molecular structure of the protein is destroyed during heating. The results indicates that the EIT system can record changes in the conductivity of egg during heating and distinguish between raw egg and heated egg.

### V. CONCLUSIONS

This paper developed a portable, low-cost, high-precision EIT system based on Red Pitaya STEMLab for families and individuals. The results are as follows:

- 1) In the EIT system, Red Pitaya STEMLab fully utilized its hardware programmable control, signal generation and acquisition capabilities to implement the most functions of the EIT system. According to the test results, the output impedance of VCCS at  $f = 100$  KHz is  $Z_{out} = 726$  K $\Omega$ , which satisfies the requirements of the EIT system for the output impedance of the current source. The EIT system simultaneously controls four 16-channel analog multiplexer devices through eight Red Pitaya STEMLab digital output channels. Modules in the EIT system are all independent and can improve overall performance by improving or replacing a module.
- 2) The images are reconstructed with the data collected by the developed EIT system with the algorithm of GVSPM. The image correlation  $I_C$ , voltage error  $U_E$ , and the number of iterations  $Iter$  are used to evaluate the quality of the reconstructed images. The EIT system accurately image the polyurethane rod phantom within the frequency  $f = 300$



KHz.

- 3) The reconstructed images by the developed EIT system was compared with the commercial impedance analyzer IM3570 within frequencies of  $f = 100$  KHz. The maximum difference of the image correlation between Red Pitaya STEMLab and IM3570 is 5.36%.
- 4) The developed EIT system was also used to image the change in conductivity during heating of the eggs. These results verified that the developed portable EIT system with Red Pitaya STEMLab could measurement the biological tissue in a high accuracy at low cost.

## REFERENCES

- [1] Y. Yang, J. Jia, S. Smith *et al.*, "A Miniature Electrical Impedance Tomography Sensor and 3D Image Reconstruction for Cell Imaging," *IEEE Sensors Journal*, no. 17(2), pp. 514-523, 2016.
- [2] J. Yao, T. Koder, H. Obara *et al.*, "Spatial concentration distribution analysis of cells in electrode-multilayered microchannel by dielectric property measurement," *Biomicrofluidics*, vol. 9, no. 4, pp. 044129, 2015.
- [3] J. Yao, A. Sapkota, H. Konno *et al.*, "Noninvasive online measurement of particle size and concentration in liquid-particle mixture by estimating equivalent circuit of electrical double layer," *Particulate Science and Technology*, vol. 34, no. 5, pp. 517-525, 2015.
- [4] M. Baidillah, A. A. Iman, Y. Sun *et al.*, "Electrical Impedance Spectro-Tomography (EIST) based on Dielectric Relaxation Model," *IEEE Sensors Journal*, vol. 17, no. 24, pp. 8251-8262, 2017.
- [5] C. Tan, N. Wang, and F. Dong, "Oil-water two-phase flow pattern analysis with ERT based measurement and multivariate maximum Lyapunov exponent," *Journal of Central South University*, vol. 23, no. 1, pp. 240-248, 2016.
- [6] C. Tan, Y. Xu, and F. Dong, "Determining the boundary of inclusions with known conductivities using a Levenberg-Marquardt algorithm by electrical resistance tomography," *Measurement Science and Technology*, vol. 22, no. 10, pp. 104005, 2011.
- [7] C. Tan and F. Dong, "Modification to mass flow rate correlation in oil-water two-phase flow by a V-cone flow meter in consideration of the oil-water viscosity ratio," *Measurement Science & Technology*, vol. volume 21, no. 21, pp. 45403-45414(12), 2010.
- [8] C. Tan, F. Dong, and M. Wu, "Identification of gas/liquid two-phase flow regime through ERT-based measurement and feature extraction," *Flow Measurement & Instrumentation*, vol. 18, no. 5, pp. 255-261, 2007.
- [9] S. Ren, M. Soleimani, Y. Xu *et al.*, "Inclusion boundary reconstruction and sensitivity analysis in electrical impedance tomography," *Inverse Problems in Science & Engineering*, no. 4, pp. 1-25, 2017.
- [10] J. F. Yao and M. Takei, "Application of Process Tomography to Multiphase Flow Measurement in Industrial and Biomedical Fields: A Review," *IEEE Sensors Journal*, vol. 17, no. 24, pp. 8196-8205, 2017.
- [11] V. E. Arpinar and B. M. Eyuboglu, "Microcontroller controlled, multifrequency electrical impedance tomograph," pp. 2289-2291 vol.3.
- [12] A. Ruiz-Vargas, J. W. Arkwright, and A. Ivorra, "A portable bioimpedance measurement system based on Red Pitaya for monitoring and detecting abnormalities in the gastrointestinal tract," pp. 150-154.
- [13] Y. Yang and J. Jia, "A multi-frequency electrical impedance tomography system for real-time 2D and 3D imaging," *Review of Scientific Instruments*, vol. 88, no. 8, pp. 085110, 2017.
- [14] A. J. Wilson, P. Milnes, A. R. Waterworth *et al.*, "Mk3.5: a modular, multi-frequency successor to the Mk3a EIS/EIT system," *Physiological Measurement*, vol. 22, no. 1, pp. 49-54, 2001.
- [15] A. Mcewan, A. Romsauerova, R. Yerworth *et al.*, "Design and calibration of a compact multi-frequency EIT system for acute stroke imaging," *Physiological Measurement*, vol. 27, no. 5, pp. S199, 2006.
- [16] H. Wi, H. Sohal, A. L. Mcewan *et al.*, "Multi-Frequency Electrical Impedance Tomography System With Automatic Self-Calibration for Long-Term Monitoring," *IEEE Transactions on Biomedical Circuits & Systems*, vol. 8, no. 1, pp. 119-128, 2014.
- [17] T. K. Bera and J. Nagaraju, "Surface electrode switching of a 16-electrode wireless EIT system using RF-based digital data transmission scheme with 8 channel encoder/decoder ICs," *Measurement*, vol. 45, no. 3, pp. 541-555, 2012.
- [18] Y. Zhang, R. Xiao, and C. Harrison, "Advancing Hand Gesture Recognition with High Resolution Electrical Impedance Tomography," pp. 843-850.
- [19] S. Pullett, A. Adler, M. Kott *et al.*, "Regional lung opening and closing pressures in patients with acute lung injury," *Journal of Critical Care*, vol. 27, no. 3, pp. 323.e11, 2012.
- [20] A. S. Tucker, R. M. Fox, and R. J. Sadleir, "Biocompatible, high precision, wideband, improved Howland current source with lead-lag compensation," *IEEE Transactions on Biomedical Circuits & Systems*, vol. 7, no. 1, pp. 63-70, 2013.
- [21] J. Anudev and I. J. Raglend, "Analytical study of howland current source model," pp. 314-318.
- [22] A. A. Al-Obaidi and M. Meribout, "A new enhanced Howland voltage controlled current source circuit for EIT applications," pp. 327-330.
- [23] P. Bertemes-Filho, B. H. Brown, and A. J. Wilson, "A comparison of modified Howland circuits as current generators with current mirror type circuits," *Physiological Measurement*, vol. 21, no. 1, pp. 1, 2000.
- [24] P. Bertemesfilho, B. H. Brown, and A. J. Wilson, "A comparison of modified Howland circuits as current generators with current mirror type circuits," *Physiological Measurement*, vol. 21, no. 1, pp. 1, 2000.
- [25] X. Li, D. Feng, and Y. Fu, *Analysis of constant-current characteristics for current sources*, 2012.
- [26] H. Bian, Jiang-tao, YANG *et al.*, "Theoretical analysis method for Howland current source design," *Journal of Measurement Science & Instrumentation*, vol. 03, no. 3, pp. 287-293, 2012.
- [27] C. W. Denyer, F. J. Lidgley, Q. S. Zhu *et al.*, "A high output impedance current source," *Physiological Measurement*, vol. 15 Suppl 2a, no. 2A, pp. A79-82, 1994.
- [28] B. H. Brown, D. C. Barber, W. Wang *et al.*, "Multi-frequency imaging and modelling of respiratory related electrical impedance changes," *Physiological Measurement*, vol. 15 Suppl 2a, no. 2A, pp. A1-12, 1994.
- [29] Y. Zhang and C. Harrison, "Tomo: Wearable, Low-Cost Electrical Impedance Tomography for Hand Gesture Recognition," pp. 167-173.
- [30] M. Vauhkonen, D. Vadsz, P. A. Karjalainen *et al.*, "Tikhonov regularization and prior information in electrical impedance tomography," *IEEE Transactions on Medical Imaging*, vol. 17, no. 2, pp. 285-93, 1998.
- [31] X. Liu, J. Yao, Y. Cui *et al.*, "Image Reconstruction under Contact Impedance Effect in Micro Electrical Impedance Tomography Sensors," *IEEE Transactions on Biomedical Circuits and Systems*, 2018.
- [32] G. Y. Dong, H. Endo, S. Hayano *et al.*, "GVSPM for reconstruction in electrical impedance tomography," *Magnetics IEEE Transactions on*, vol. 39, no. 3, pp. 1630-1633, 2003.
- [33] M. Khalighi, B. V. Vahdat, M. Mortazavi *et al.*, "DESIGN AND IMPLEMENTATION OF PRECISE HARDWARE FOR ELECTRICAL IMPEDANCE TOMOGRAPHY (EIT)," *Iranian Journal of Science and Technology - Transactions of Electrical Engineering*, vol. 38, no. E1, pp. 1-20, 2014.